PAPER

Check for updates

Innovative polycaprolactone/graphitic carbon nitride composite coatings: enhancing the antibacterial properties of nanoporous alumina membranes

Ahmed N. Emam, [ID] * Lamyaa Osama, Hanan H. Beherei and Mostafa Mabrouk [ID] *

Despite the intensive need for antifouling coatings against bacterial contamination, issues remain. Herein, we present a novel approach to enhance the antifouling and antibacterial properties of nanoporous alumina membranes (ALNPMs) by coating them with polycaprolactone (PCL) and graphitic carbon nitride (g-C_3N_4). A porous PCL coating, functionalized with NHS/EDC, was deposited via a spin-coating technique onto the ALNPMs, incorporating g-C_3N_4 at ratios of 1 and 2 wt%. The coated membranes were characterized using SEM/EDX, TEM, FTIR/ATR, XRD, and contact angle measurements. The results revealed that the addition of g-C_3N_4 increased the hydrophilicity of the coated membranes. Contact angles reached 68.5° for 1 wt% and 78.9° for 2 wt% PCL containing g-C_3N_4 coatings compared to pure PCL at 96°. The antifouling properties of the coating were tested by determining the bovine serum albumin (BSA) adsorption and pH stability. At a higher content of g-C_3N_4 (2 wt%), the membrane showed lower BSA adsorption over 14 days (28%) alongside structural integrity. Antibacterial properties against *Escherichia coli* (*E. coli*) and *Staphylococcus aureus* (*S. aureus*) showed an increase in inhibition upon incorporation of g-C_3N_4. The membrane with 2 wt% g-C_3N_4 showed the highest effectiveness with inhibition zones of 36 and 30 mm for *E. coli* and *S. aureus*, respectively. Possible mechanisms for this improvement include increased hydrophilicity, physical destruction of bacterial membranes, and photocatalytic reactive oxygen species generation. Overall, PCL/g-C_3N_4 coatings significantly improve antifouling and antibacterial functionalities, which make them promising candidates for use in membrane technology for biomedical applications.

1. Introduction

The fouling effects that arise when membranes interact with other media significantly challenge membrane technologies, despite their revolutionary status in most fields.[1,2] Fouling occurs in biomedical applications when devices interact with physiological fluids, which deteriorates their performance and may lead to complications in patients.[1,3,4] Similarly, in industrial and environmental wastewater treatment applications, membrane fouling reduces filtration efficiency and increases operational costs, evidencing the extreme necessity of new antifouling strategies in these diverse applications.[5–8] Nanoporous membranes are a big step forward in separation technology because their pores can be precisely controlled, and they can be as small as a few nanometers or as large as hundreds of

nanometers. This approach allows molecules to move and be filtered at the nanoscale level.[9–12] In this group, alumina nanoporous membranes (ALNPMs) are critical since they have a special hexagonal pore structure, are extremely heat stable, are chemically resistant, and have controllable pore sizes.[13–15] Most of these membranes are generally prepared using two-step anodization of pure aluminum, and this technique leads to well-organized, straight, cylindrical, and highly uniform pores.[14,16,17] Recent advancements in ALNPMs have focused on enhancing their functionality through surface treatment. Such methods include special coatings, incorporation of nanoparticles, and the creation of smart surfaces responsive to changes.[18–21] They are now used in different fields like water purification (where they are excellent at getting rid of impurities and microorganisms), biotechnology (as platforms for drug delivery and protein separation), energy systems (especially fuel cells and batteries), and environmental remediation (where they help with selective gas separation and catalysis).[22–25] However, these membranes often face challenges related to fouling and bacterial contamination, which significantly affect their performance and longevity.[26–28]

Refractories, Ceramics and Building Materials Department – Advanced Material Technology & Mineral Resources Research Institute, National Research Centre (NRC), El Bohouth St., Dokki, 12622 Cairo, Egypt.
E-mail: ahmed.gsc.ndp@gmail.com, an.emam@nrc.sci.eg, mostafamabrouk.nrc@gmail.com

Antifouling coatings have appeared as one of the most important recent developments in membrane technology. They behave like protective layers to hinder fouling and enhance membrane efficiency. The mechanisms concerned with such coatings involve hydrophilic surfaces, antimicrobial agents, and photocatalytic properties to reduce foulant adhesion without compromising separation functionality. Key benefits include lower operational expenses, reduced cleaning needs, extended membrane life, and improved efficiency.[16,29–32] Advanced modern versions with graphitic carbon nitride (g-C_3N_4), zwitterionic polymers, and poly ε-caprolactone (PCL) also provide excellent durability and are environmentally friendly. Recent developments yielded multifunctional surfaces featuring self-cleaning properties with smart responsive capabilities; thus, these coatings have become highly valuable in a wide range of applications from water treatment to biotechnology. This technology has substantially advanced membrane processes by enabling precise control of fouling, thereby enhancing long-term performance, sustainability, and cost-effectiveness in separation applications.[33–40]

PCL is a novel coating material for ALNPMs and has excellent antifouling properties due to its biodegradability, biocompatibility, and functionalization possibilities.[41] Its semi-crystalline structure enables stable coatings, while its adjustable degradation rate allows the controlled release of active agents that enhance the antifouling properties.[42,43] Based on these findings, PCL-coated membranes can reduce protein adsorption by up to 75%. Furthermore, incorporating nanomaterials such as graphene oxide or silver nanoparticles, together with copolymerization with hydrophilic segments, further improves resistance to organic fouling and bacterial adhesion.[44–47] In summary, PCL coatings represent a promising platform for future separation technologies, with ongoing research providing the latest developments.

Another noteworthy material is graphitic carbon nitride (g-C_3N_4) due to its fascinating two-dimensional configuration and outstanding properties, including very high chemical stability, biocompatibility, and photocatalytic activity.[48,49] When deposited on ALNPMs, g-C_3N_4 brings multiple functions to overcome all major drawbacks observed in conventional membrane systems.[50,51] In the meantime, g-C_3N_4 functional groups that contain nitrogen provide enhanced surface hydrophilic interactions for forming a protective water layer, reducing organic fouling. Apart from this, the photocatalytic properties contributed by g-C_3N_4 promote self-cleaning by degrading organic contaminants and inactivating bacteria under visible light irradiation.[52–54]

To the authors' knowledge, there have not been any studies investigating the effectiveness of g-C_3N_4/PCL-based coatings in preventing particles from sticking to nanoporous membranes. Thus, the current study aimed to integrate PCL, a biodegradable polyester, with g-C_3N_4, further improving the coating's durability and providing more functionalities. PCL's excellent film-forming ability and controlled degradation features make it possible for antimicrobial agents to be released over time, while the membrane's structure stays intact. Therefore, a porous coating layer made of PCL, modified with an NHS/EDC complex, was applied to the ALNPMs prepared using a spin coating method. To improve the coating's durability and antifouling and antibacterial functionalities, g-C_3N_4 was added at two different ratios, 1 and 2 wt%, to the PCL–NHS/EDC polymer matrix in the current experiment. In addition, the pristine ALNPMs and the coating materials were characterized before and after coating using several characterization techniques, such as SEM/EDX, TEM, FTIR/ATR, XRD, and contact angle measurements. Moreover, antifouling tests were performed according to the ion concentrations of the artificial cerebrospinal fluid (A-CSF). Finally, the antifouling features were tested against two different bacterial species.

2. Experimental

2.1. Materials

The ALNPMs were prepared *via* electrochemical anodization according to previous work by Osama *et al.*[25] The following materials were used for producing the coating layers: urea (CH$_4$N$_2$O, 99%; Merck Chemicals Company, Massachusetts, USA), poly ε-caprolactone (PCL, CH$_3$(C$_6$H$_{10}$O$_2$)$_n$CH$_3$, 80 000, 99%; Sigma-Aldrich, Germany), dichloromethane (DCM, suitable for HPLC, CH$_2$Cl$_2$, ≥99.8%; Sigma-Aldrich, Germany), N,N-dimethylformamide (DMF; Merck, Gangnam-gu, Seoul, South Korea), N-hydroxysuccinimide (NHS, 98+%; Acros Organics, Shanghai, China), and 1-ethyl-3-(3-dimethylaminopropyl)carbodiimide hydrochloride (EDC, 97%; Acros Organics, Geel, Belgium).

2.2. Methodology

2.2.1. Preparation of graphitic carbon nitride (g-C_3N_4) nanosheets. Graphitic carbon nitride (g-C_3N_4) was synthesized by thermal decomposition treatment as previously reported.[55–57] Pristine g-C_3N_4 was prepared by heating urea in a furnace. In detail, a certain amount of urea was put into a porcelain crucible, which was first heated to 550 °C at a heating rate of 10 °C min^{-1} and then kept at 550 °C for 1 h. After the reaction, the alumina crucible was cooled down naturally to room temperature. The as-prepared g-C_3N_4 was collected and ground into a powder, as shown in Fig. 1. To obtain g-C_3N_4 nanosheets, the as-prepared bulk g-C_3N_4 was again thermally treated using the above heating protocol for further thermal exfoliation of stacked bulk g-C_3N_4 into nanosheets, as shown in Fig. 1.[58]

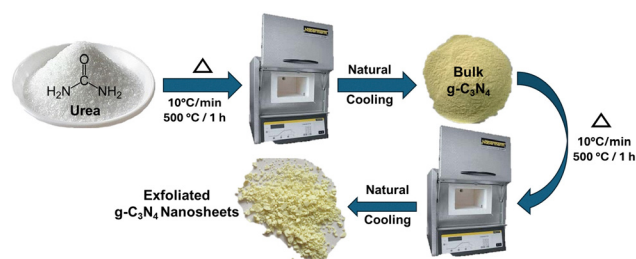**Fig. 1** Scheme for the preparation of exfoliated g-C_3N_4 nanosheets.

2.2.2. Preparation of PCL/g-C$_3$N$_4$ based coating materials. First, 1.5 g of PCL was dissolved in 20 mL of DCM with vigorous stirring. In a separate container, g-C$_3$N$_4$ was dispersed in 5 mL of DMF at concentrations of 1 or 2 wt% by weight relative to PCL and stirred vigorously for 30 minutes. This g-C$_3$N$_4$ dispersion was then added to the PCL solution and stirred vigorously for another 30 minutes to obtain a homogeneous mixture.

Next, to activate the surface and convert the carboxylic groups on PCL into amine-reactive esters, a solution composed of 20 mM EDC and 50 mM NHS was prepared in 5 mL of DMF. This solution was added to each PCL alone and the PCL/g-C$_3$N$_4$ mixture, respectively. Then the mixture was sonicated and stirred for 1 h. Finally, the coating materials (PCL or PCL/g-C$_3$N$_4$) were transferred to a vacuum spin-coater. Using a syringe, 2 mL of the polymer blend was applied to the surface of ALNPMs. The spin-coater was run for 2-min cycles at 200 rpm. The coated membranes were then left to dry overnight at room temperature (Fig. 2).

2.3. Characterization

2.3.1. Characterization of g-C$_3$N$_4$ nanosheets. High-resolution transmission electron microscopy (HR-TEM; JEOL JEM 2100, Tokyo, Japan) was used for the morphological studies regarding the shape and size. For this study, 0.01 g of g-C$_3$N$_4$ was added to 10 mL of distilled water to obtain a dilute suspension using ultrasonic vibrations. Drops of this suspension were placed on copper grids, air-dried on filter paper, and then analyzed.

Chemical composition and the type of functional group were identified by two complementary FTIR techniques. g-C$_3$N$_4$ nanosheets were analyzed using FT-IR employing a Thermo Nicolet 6700 ATR/FTIR spectrophotometer at 25 °C with a resolution of 4 cm^{-1}. The samples for the analysis were prepared by mixing with KBr powder at a 5 : 195 mg ratio and pressing into uniform disks.

Crystallographic analysis of g-C$_3$N$_4$ nanosheets was performed on a Bruker D8 advanced X-ray powder diffractometer using Cu Kα radiation (Kα1 = 1.54060 Å, Kα2 = 1.5444 Å). Data were collected from 10° to 70° in steps of 2°.

2.3.2. Characterization of coated ALNPMs. The surface morphology and elemental composition of uncoated and coated ALNPMs were investigated by SEM–EDX analysis (JXA-840A, JEOL, Tokyo, Japan) at a 15 kV accelerating voltage. The samples were then mounted on stainless-steel holders using carbon tape and sputter-coated with gold in preparation for microscopic examination and microstructural analysis.

The powder samples of pristine ALNPMs and PCL/g-C$_3$N$_4$-coated ALNPMs were analyzed using a Thermo Nicolet 6700 FTIR spectrophotometer at 25 °C with a resolution of 4 cm^{-1}. The membrane samples were analyzed by FTIR/ATR spectroscopy using a Nicolet 6700 (Thermo-Fisher, Norristown, PA, USA). All spectra were recorded within the wavenumber range of 4000 to 500 cm^{-1}.

Finally, the wettability of the surface significantly affects the antifouling properties of the membranes; the hydrophilicity of the surface is crucial for investigating the various interactions of different foulants on newly fabricated membranes. Hydrophilicity was evaluated from the static water contact angle (θ), defined as the angle formed between a vertically deposited water droplet and the membrane surface. The surface wettability of the alumina nanoporous membranes was measured using a Theta Lite optical tensiometer contact angle analyzer (Nanoscience Instruments, USA).

2.4. Stability of coatings under A-CSF conditions

The pH of artificial cerebrospinal fluid (A-CSF) was measured before and after coating by immersing the ALNPMs measuring 0.7 × 0.7 cm^2. Each membrane was placed in a plastic container containing 50 mL of A-CSF and kept at 37 °C for 14 days. About 3 mL of the samples were drawn from each container at different time periods – 1, 4, 5, 7, 8, 11, and 14 days – to monitor changes in the pH level of A-CSF.

2.5. Anti-biofouling activity against microbial isolates

The antibiofouling efficiency of the membranes against the three model microorganisms was evaluated by light microscopy as reported previously: the Gram-negative bacterium *Escherichia coli* (ATCC 25922), the Gram-positive *Staphylococcus aureus* (ATCC-6538), and the fungus *Candida albicans* (ATCC 10231), which were obtained from the American Type Culture Collection, Rockville, MD, USA.[59] Prior to testing, the bacterial strains were revived by subculturing for 24 h in fresh nutrient broth. A bacterial suspension of 1 mL was mixed with 9 mL of fresh nutrient broth. The mixture was then left to sit for 4 h or until an optical density of 1.4 at 600 nm was reached. The bacterial cells were then harvested by centrifugation at 10 000 rpm for 10 min, washed with phosphate buffered saline (PBS), and standardized to a concentration of 10^7 CFU mL^{-1}.[60,61]

Membrane samples in a circular shape with dimensions of 0.88 cm^2 (0.7 mm diameter) were exposed to 10 mL of the bacterial suspension for 15 min. After incubation, the bacterial suspensions were removed and transferred to fresh tubes containing PBS. Antimicrobial effectiveness was further analyzed with a light microscope using Gram staining to distinguish between living and dead bacterial cells on the membrane
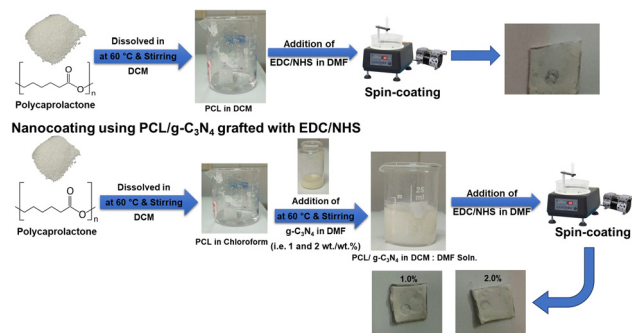

Fig. 2 Scheme for the coating of ALNPMs with PCL and PCL/g-C$_3$N$_4$ grafted with NHS/EDC.

surface. After 15 min of exposure, *E. coli*, *S. aureus*, and *C. albicans* suspensions were Gram-stained to visualize surface-adherent microorganisms. A C2 light microscope (Olympus Corporation, Tokyo, Japan) was employed for imaging, and the obtained images were compared against controls.[16,62]

2.6. Adsorption of bovine serum albumin (BSA)

The antifouling performance of coated and uncoated ALNPMs was tested by a static adsorption method using BSA in artificial cerebrospinal fluid (A-CSF, 1 g L^{-1}, pH 7.4). The membranes were cut into 0.7 cm × 0.7 cm and then coated with a composite solution containing PCL or PCL/g-C_3N_4 with two different g-C_3N_4 concentrations (*i.e.* 1 and 2 wt%). Then, the samples were immersed in BSA solution and placed in a temperature-controlled environment at 37 °C. At different intervals – after 1, 3, 5, 7, and 14 days of soaking – 3 mL was extracted and replaced by new BSA solution. The concentrations of BSA were analyzed using a JASCO V-730 UV-vis spectrophotometer at a 260 nm wavelength and obtained according to a standard curve developed in this research. All experiments involved three replicate measurements. The mean values and percentages of adsorption were calculated using eqn (1):

$$\text{BSA adsorption \%} = \frac{\left(\text{BSA}_{\text{initial}} - \text{BSA}_{\text{sample}}\right)}{\text{BSA}_{\text{initial}}} \times 100 \quad (1)$$

where $\text{BSA}_{\text{initial}}$ is the initial concentration of BSA before soaking of ALNPMs and $\text{BSA}_{\text{sample}}$ is the concentration obtained at each time interval.

2.7. Antibacterial study

In vitro assays were conducted on five membrane sample groups using Gram-positive *Staphylococcus aureus* (ATCC 29213) and Gram-negative *Escherichia coli* (ATCC 25922), obtained from the American Type Culture Collection and the U.S. Department of Agriculture, Northern Research Division. Mueller–Hinton agar was prepared with infused beef extract powder (2.0 g L^{-1}), acid digest of casein (17.5 g L^{-1}), starch (1.5 g L^{-1}), and agar (17.0 g L^{-1}). The final pH was 7.3 ± 0.1 at 25 °C. Revitalization was ensured for inoculation by a process of 24 h subculture in bacterial stock cultures kept under nutrient broth conditions. Stock cultures were maintained at 4 °C on nutrient agar slopes. The cells for active cultures were transferred into Mueller–Hinton broth and incubated at 37 °C for 24 h or at 25 °C for 48 h. The assessment was conducted by comparing the bacterial suspension to the 0.5 McFarland standard, which was prepared by mixing barium chloride and sulfuric acid until the turbidity level reached 1.5 × 10^8 CFU mL^{-1} at 625 nm.[63,64] Antimicrobial activity was evaluated by the agar well diffusion method under ambient light. A volume of 0.1 mL of standardized culture was swabbed on Mueller–Hinton agar plates. After solidification, the five membrane samples were placed as disks on the agar surface. Following 24 h of incubation at 37 °C, the diameters of inhibition zones were measured.[65,66] Sensitivity was recorded as strongly sensitive (≥28 mm), moderately sensitive (16–28 mm), weakly sensitive (12–16 mm), or resistant (<12 mm).

3. Results and discussion

3.1. Characterization of g-C_3N_4 nanosheets

The morphology, crystallographic structure and surface properties of the as-prepared exfoliated g-C_3N_4 were investigated as shown in Fig. 3. As shown in Fig. 3a, a large sheet of g-C_3N_4 with a diameter and length > 100 nm and an irregular appearance was observed. In addition, the selected area electron diffraction (SAED) pattern of the exfoliated g-C_3N_4 sample shown in Fig. 3b demonstrated a *d*-spacing of 0.335 nm, which corresponds closely to the (002) plane observed in the XRD patterns. This value is closest to the *d*-value acquired from the XRD pattern of the (002) plane of exfoliated g-C_3N_4 shown in Fig. 3c. Moreover, XRD analysis revealed two characteristic peaks: one weak peak at 2θ = 12.8° and one strong peak at 2θ = 27° (see Fig. 3c), similar to previous studies.[67,68] The diffraction peak appearing at a low angle, 12.8°, corresponds to the (100) crystallographic plane, and reflects the spacing between the flat tri-*s*-triazine units.[67,68] A strong peak centered at 27° is associated with the (002) crystallographic plane (see Fig. 3c), reflecting the interlayer stacking interactions within the conjugated aromatic system typical for graphitic materials.[67]

Finally, FTIR was used for determining the structural composition of the exfoliated g-C_3N_4 nanosheets, as shown in Fig. 3d. Indeed, within this region (1200–1600 cm^{-1}), characteristic stretching vibrational modes were observed for the conjugated CN ring. Precisely, the two important characteristic stretching bands situated at 1194 and 1681 cm^{-1} can be assigned to the amine group-C–N and C=N/secondary amide (C=O), respectively. The exfoliated g-C_3N_4 nanosheet exhibited a characteristic absorption peak at 809 cm^{-1}, which was assigned to the breathing mode of triazine units. Three broad absorption bands within the 3000–3500 cm^{-1} region corresponded to the stretching of N–H and O–H, as previously
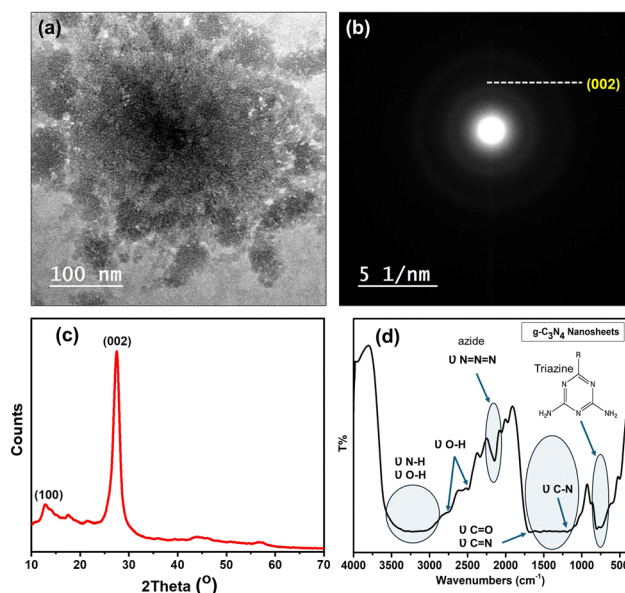

Fig. 3 (a) TEM image, (b) SAED pattern, (c) XRD pattern and (d) FT-IR spectrum of the as-prepared g-C_3N_4.

reported.[67] Besides, three stretching vibrations were observed at 2742, 2500, and 2145 cm^{-1}, which could be assigned to –OH and azide (N=N=N) functional groups.

3.2. Characterization of coated ALNPMs

3.2.1. Scanning electron microscopy. Fig. 4 and 5 show the SEM/EDX images of the pristine ALNPMs as well as the microporous 3D structures of the fabricated coating with PCL and PCL/g-C$_3$N$_4$ grafted with an NHS/EDC complex. Fig. 4a presents a highly ordered, uniform distribution of pores for pristine ALNPMs with a mean pore size of 53.6 nm, as shown in Fig. 4b. It can be seen from the SEM micrograph that the structure is honeycomb-like, typical of anodized aluminium membranes.[69–71]

Moreover, EDX analysis results presented in Fig. 4c confirm the membrane composition with predominant elements being oxygen (60.53 at%) and aluminum (39.47 at%), consistent with the Al$_2$O$_3$ structure typical of anodized membranes. This is an ordered structure resulting from the self-organizing nature of the anodization process in which pore formation occurs *via* controlled oxide dissolution.

PCL-coated ALNPMs showed a great change in morphology upon coating with poly ε-caprolactone. SEM images that are presented in Fig. 4d show that the mean pore size increased to
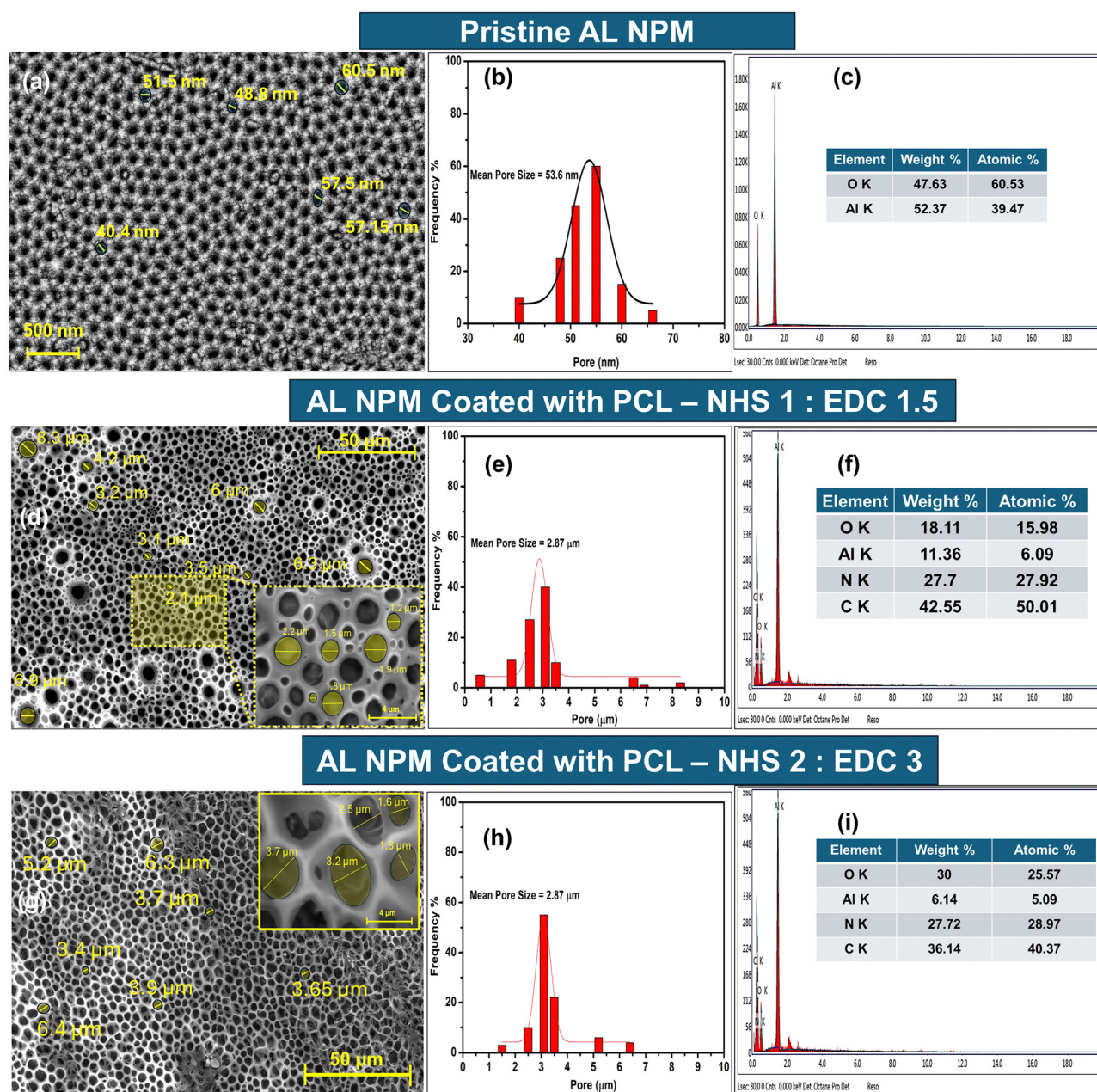

Fig. 4 SEM images (a), (d), and (g), pore size distribution histograms (b), (e), and (h), and EDX profiles (c), (f), and (i) of a pristine alumina nanoporous membrane and alumina nanoporous membranes coated with PCL.
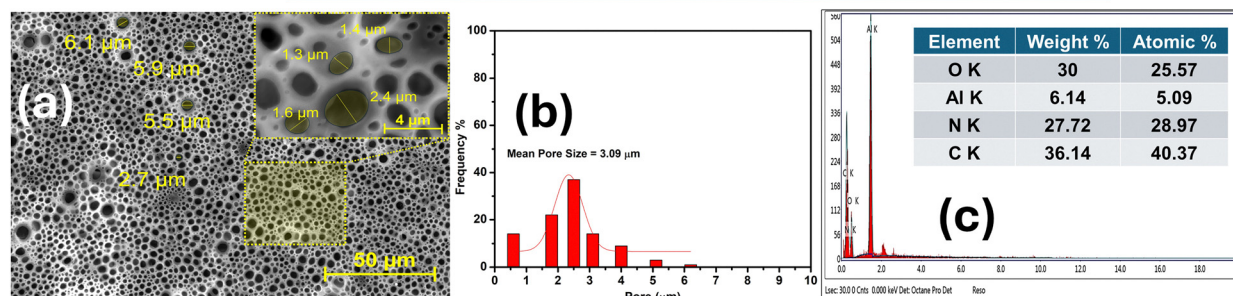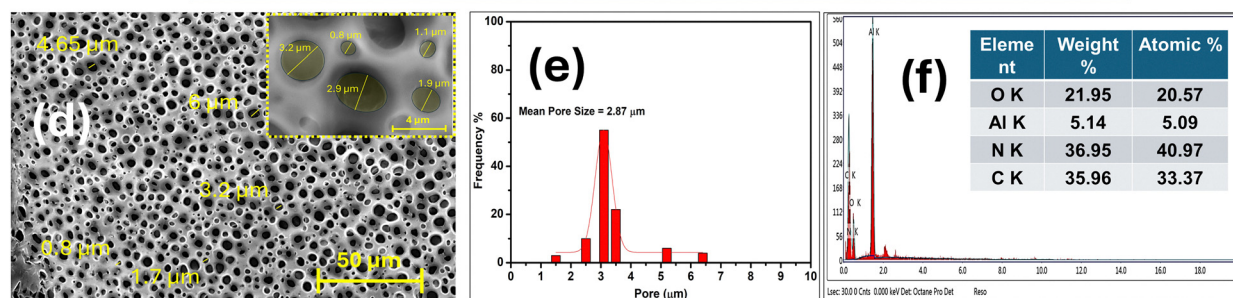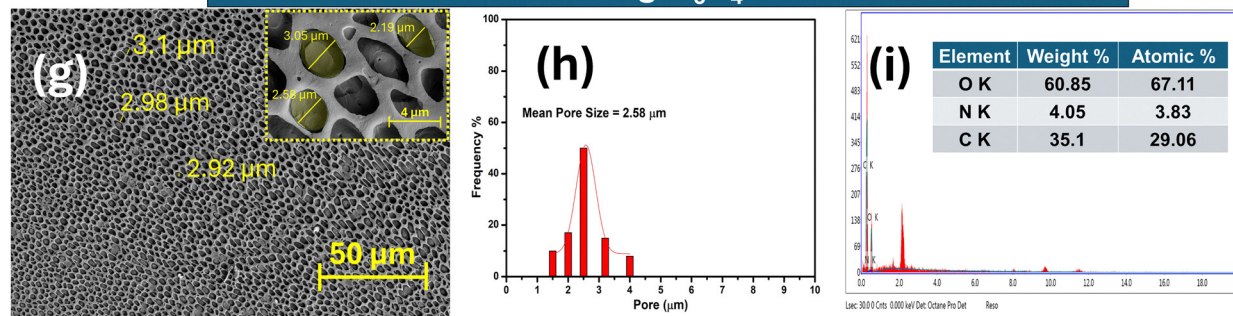
Fig. 5 SEM images (a), (d), and (g), pore size distribution histograms (b), (e), and (h), and EDX profiles (c), (f), and (i) of an alumina nanoporous membrane coated with the PCL/g-C$_3$N$_4$ composite.

2.87 µm (see Fig. 4e), indicating pore expansion and covering of the polymer. EDX analysis shows that 50.01 at% of carbon and 27.92 at% of nitrogen were introduced, while the aluminum content dropped to 6.09 at%, which reflects effective polymer deposition, as shown in Fig. 4f. In addition, the use of two different ratios of NHS : EDC, 1 : 1.5 and 2 : 3, yields different coating results, although the latter is more homogeneous (see Fig. 4f).

Furthermore, adding g-C$_3$N$_4$ to the PCL coating significantly alters its morphology and composition. SEM images shown in Fig. 5a, d and g reveal that the pore size varies between 2.87 and 3.1 µm depending on the g-C$_3$N$_4$ concentration (1–2 wt% w.r.t. PCL wt%) and the NHS : EDC ratio. EDX analysis reveals that, for some samples, the nitrogen content increases up to 40.97 at%, which confirms the successful integration of g-C$_3$N$_4$. The 2 wt% g-C$_3$N$_4$ samples have a more homogeneous distribution and higher surface roughness, which might be useful in applications requiring high surface area.

The thickness of the pristine alumina porous membrane measured using a digital micrometer was approximately 0.01 mm. In contrast, the coated membranes showed increased thickness values: the thickness of PCL grafted with an NHS : EDC ratio of 1 : 1.5 was approximately 0.012 mm, while that of the PCL/g-C$_3$N$_4$ composites with an NHS : EDC ratio of 2 : 3 was approximately 0.015 mm for a 1 wt% loading and approximately 0.016 mm for a 2 wt% loading. These measurements indicate a progressive increase in membrane thickness with the addition of coating layers and increasing g-C$_3$N$_4$ content.

3.2.2. FTIR analysis of ALNPMs before and after coating. Fig. 6 shows the FT-IR spectra of ALNPMs coated with PCL and PCL/g-C$_3$N$_4$ (1 and 2 wt%). Coating of the alumina membrane with PCL resulted in the appearance of characteristic absorption bands of the PCL polymer. The sharp peak at 1720 cm^{-1} was assigned to the C=O stretching vibration of the ester carbonyl group of PCL. The absorptions at 2950 and 2870 cm^{-1} correspond to asymmetric and symmetric C–H
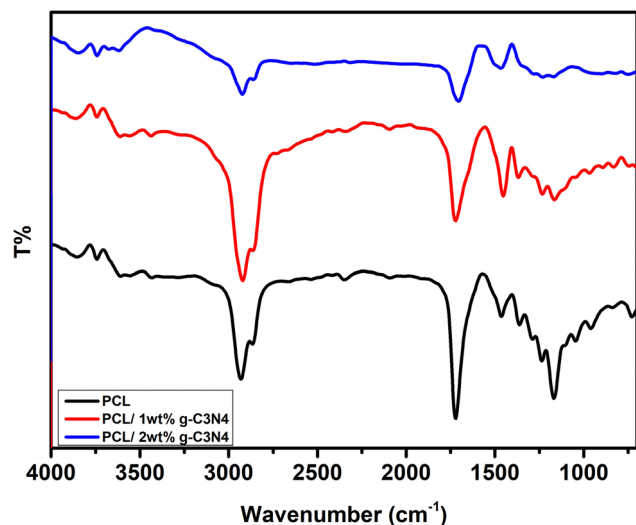
Fig. 6 FT-IR/ATR spectra and values of pristine ALNPMs and coated membrane surfaces.

stretching of methylene groups along the main chain of PCL. Thus, in an ester, the absorption band *ca.* 1240 cm^{-1} is assigned to the C–O–C stretching, while the peaks located between 1200 and 1100 cm^{-1} are assigned to the C–C–O stretching.

The incorporation of g-C$_3$N$_4$ within the PCL polymeric coating matrix at a ratio of 1 wt% showed similar features compared to the coating with PCL only, which confirms that the addition of a small amount of g-C$_3$N$_4$ does not change the structure of PCL significantly (see Fig. 6, red line). Small shifts and changes in the relative intensities of some of the characteristic peaks for PCL reflect slight interactions between PCL and the filler, while more pronounced changes are observed in the FT-IR spectrum of PCL upon increasing the content of g-C$_3$N$_4$ to 2 wt% compared to PCL only, as shown by a blue line in Fig. 6. In this context, the slight shift and lower intensity of the ester carbonyl peak at 1720 cm^{-1} may indicate some interactions between PCL and the higher content of g-C$_3$N$_4$. Changes in the relative intensities of the peaks in the 1200–1100 cm^{-1} region correspond to the C–C–O vibrations. This probably indicates that a higher concentration (2 wt%) of g-C$_3$N$_4$ exerts a greater impact on the structure and interactions within PCL in the composite.

3.2.3. Contact angle. Fig. 7a and b show the change in contact angle of alumina nanoporous membranes (AL NPMs) coated with three different polymeric compositions: pure polycaprolactone, PCL with 1 wt% g-C$_3$N$_4$, and PCL with 2 wt% g-C$_3$N$_4$. Contact angle measurement is a key method for assessing surface wettability, which is directly related to antifouling properties in membrane applications.[72,73] Generally, a lower contact angle indicates higher hydrophilicity, which is desirable for antifouling performance because it reduces the adhesion of hydrophobic foulants.[74–76]

As shown in Fig. 7a, the pristine ALNPMs displayed a lower contact angle of about 44.4°, while upon coating of ALNPMs with PCL-grafted NHS/EDC (see Fig. 7b), the contact angle

reached about 96°, showing a hydrophobic surface. PCL itself is a hydrophobic polymer, and therefore it has a relatively high water contact angle, which may increase the likelihood of fouling through strong hydrophobic interactions with contaminants in the aqueous environment.[76,77] As can be seen from Fig. 7c, upon loading of 1 wt% g-C$_3$N$_4$ into the PCL matrix, a significant reduction to 68.5° shows improved surface hydrophilicity. This improvement in hydrophilicity may be attributed to the presence of g-C$_3$N$_4$ containing polar functional groups such as amine and hydroxyl groups. Such functional groups tend to increase the affinity of water and reduce fouling due to minimal hydrophobic interactions with contaminants.[76,78,79] Finally, further increasing the concentration of g-C$_3$N$_4$ to 2 wt% results in a slightly higher contact angle of 78.9°, as shown in Fig. 7d. Even though this surface is still more hydrophilic than pure PCL, this increase in the contact angle with respect to the sample containing 2 wt% g-C$_3$N$_4$ can be attributed to the tendency of g-C$_3$N$_4$ particles to agglomerate at higher concentrations. This aggregation could lead to a reduction in the uniform distribution of hydrophilic functional groups on the membrane surface, thereby diminishing the overall hydrophilicity.[80]

Theoretically, hydrophilic coatings reduce the adhesion of microorganisms, proteins, and other foulants due to the reduced interaction between the surface and foulant. This is because hydrophilic surfaces have a higher affinity for water; thus, a hydration layer prevents contact between the surface and foulants.[81–84]

Statistically, contact angle analysis using the OriginPro 8.0 program showed significant variability across treatment groups (one-way ANOVA, $p < 0.001$), as shown in Fig. 7e. PCL grafting *via* NHS/EDC chemistry enhanced surface hydrophobicity significantly, with contact angles increasing from $44.0 \pm 2.2°$ (baseline) to $96.0 \pm 4.8°$ ($p < 0.001$). Incorporation of 1 wt% g-C$_3$N$_4$ reduced the contact angle to $68.5 \pm 3.425°$ ($p < 0.001$ compared to PCL), and the incorporation of 2 wt% g-C$_3$N$_4$ reduced the contact angle to $78.9 \pm 3.945°$. All modified surfaces showed significantly greater contact angles compared to the unmodified control (all $p < 0.001$), indicating that surface hydrophobicity can be controlled by g-C$_3$N$_4$ incorporation.

3.2.2. Mechanism underlying optimal performance with g-C$_3$N$_4$ loading. At 2 wt% loading, g-C$_3$N$_4$ nanoparticles are well-integrated and homogeneously dispersed in the PCL matrix. SEM/EDX characterization (Fig. 5) shows a uniform coating with a high nitrogen content (up to ~ 40.97 at% N) on the membrane surface, confirming successful incorporation of g-C$_3$N$_4$. The 2 wt% g-C$_3$N$_4$ sample exhibits a more homogeneous distribution of nanoparticles and increased surface roughness relative to lower loadings. The mean pore size of the coated membrane remains on the order of a few microns (~ 2.9–3.1 μm) for both 1% and 2% loadings, indicating that the coating uniformly covers the ALNPM without blocking its porous structure.[85] The higher surface roughness observed at 2 wt% correlates with the greater effective surface area and the formation of an "unusual topography" that is unfavorable for
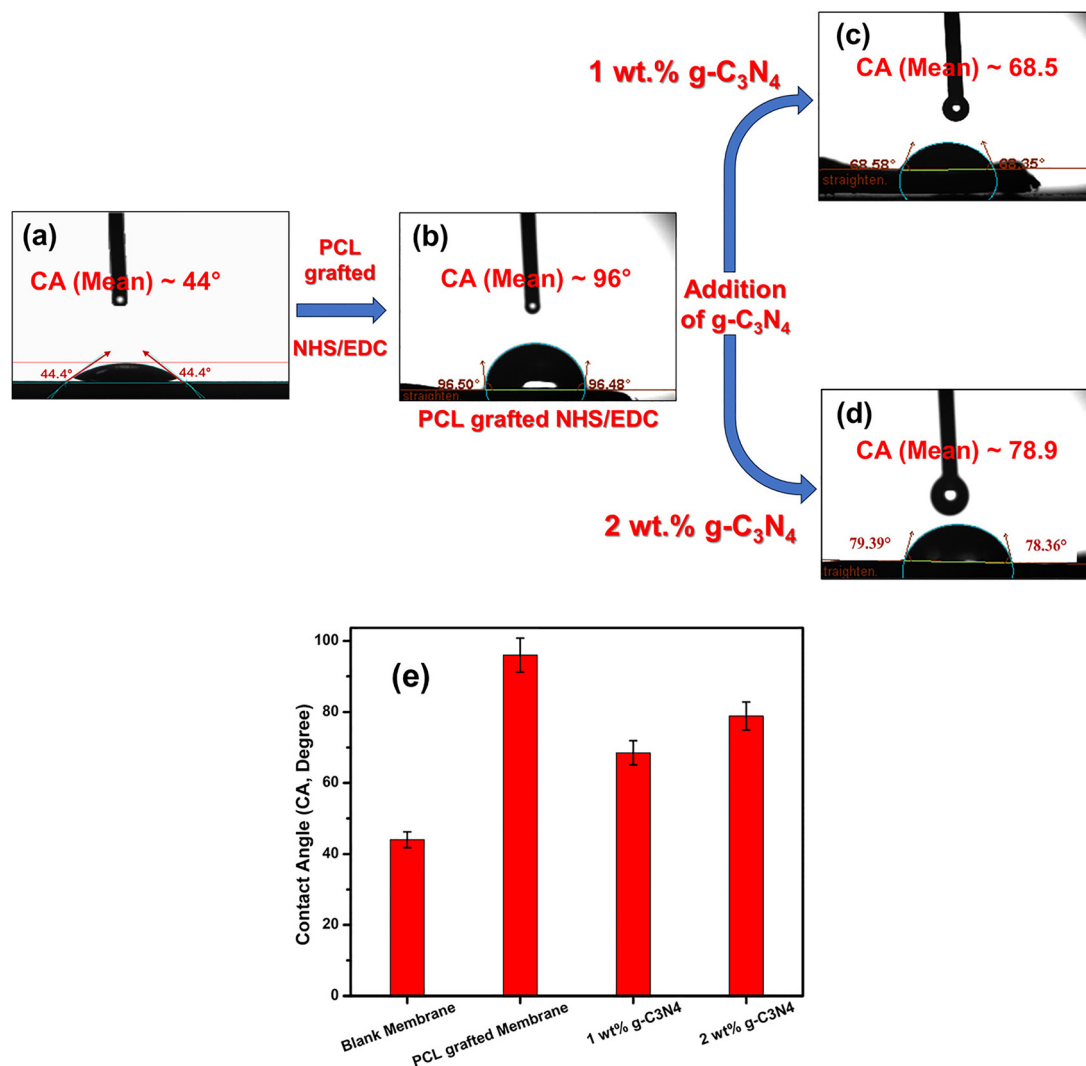
Fig. 7 (a)–(d) Contact angle images and values of pristine ALNPMs and coated membrane surfaces. (e) Changes in the contact angle values of pristine ALNPMs and coated membrane surfaces.

foulant adhesion. A rough, nano-textured coating can reduce the contact area available for bacterial cells or proteins to attach and can even physically damage microbial cell membranes upon contact.[86] In the present case, the g-C_3N_4/PCL composite with 2 wt% loading likely produces nano-protuberances and a heterogenous surface landscape, as shown in the SEM images (Fig. 5a, d and g, respectively), which may contribute to the mechanical disruption of bacteria (analogous to the bactericidal effect of nanostructured surfaces) and also hinder the stable deposition of proteins. This conclusion agrees with the literature on surface morphology effects – creating micro/nanostructured coatings is known to impede protein adsorption and biofilm formation. The 2 wt% g-C_3N_4 coating provides an optimal surface morphology for antifouling: it is sufficiently rough and uniformly covered with nanoparticles such that proteins and microbes encounter a discontinuous, water-sheathed interface, but it avoids large agglomerates or defects that might occur at excessive filler loadings.[87,88]

Furthermore, even dispersion at 2 wt% leads to the availability of more active sites on the membrane. Each g-C_3N_4 nanosheet acts as a catalytic and functional unit, and uniform dispersion increases the accessible surface area of g-C_3N_4. If it were greater with poor dispersion, nanoparticles could agglomerate and reduce the effective surface area (since only the outside of large agglomerates would be in contact with surroundings). The fact that a 2 wt% loading is better in terms of performance than 1 wt% suggests that at 1 wt% the g-C_3N_4 coverage or active site density was too low to fully cover the membrane or establish a continuous network of active sites, whereas 2 wt% reaches a point where g-C_3N_4 is both abundant and still uniformly dispersed. Further FTIR analysis showed greater changes in PCL's peaks at 2 wt% than that at 1 wt%, indicating more polymer–filler interactions at the higher loading. This is an indication that 2 wt% g-C_3N_4 remains well incorporated within the PCL matrix (possibly aided by the NHS/EDC grafting chemistry that covalently attaches PCL

chains), rather than undergoing phase separation. Good integration prevents particle leaching and maintains the structural integrity of the coating, as supported by the durability of performance for 14 days and minimal pH drift in cerebrospinal fluid (only a minimal decline in pH for 2% g-C$_3$N$_4$ owing to surface proton interactions). In summary, 2 wt% is the optimal concentration because it achieves a high density of g-C$_3$N$_4$ nanosheets that are well dispersed at the rough, high-surface-area interface, avoiding aggregation or matrix disruption that can occur at higher filler concentrations.[87,88]

3.3. Stability of coatings under CSF conditions

Fig. 8 shows the pH profiles *versus* time over 14 days for ALNPMs coated with three different compositions of PCL composites (0, 1, and 2 wt% g-C$_3$N$_4$). At an early stage, all the samples exhibited pH values close to 7.4, which is almost the same as the physiological pH of natural CSF. This is important for biomedical applications since most physiological conditions usually remain within this range. Over the first 4 days, all the compositions exhibited a relatively stable pH in the range of 7.2–7.4, which indicates excellent initial stability of the composite coatings. Starting from day 6, a gradual decrease in pH was observed, with the most evident drop observed during days 8–10. Such a drop in pH can be explained by several mechanisms.

Among them, the hydrolytic degradation of PCL produces carboxylic acid end groups, contributing to the acidification of the medium. This finding is consistent with earlier studies conducted on PCL-based biomaterials.[89–91] The addition of g-C$_3$N$_4$ does not lead to a striking change in the pH profile, while 2 wt% g-C$_3$N$_4$ presents slightly lower pH values compared to 0 and 1 wt% beyond 8 days. This may be due to the surface chemistry of g-C$_3$N$_4$ and interactions with the fluid surroundings, where g-C$_3$N$_4$ can participate in proton transfer processes at the solid–liquid interface and can thus affect the local pH environment.[92] On the 14th day, all the compositions converge
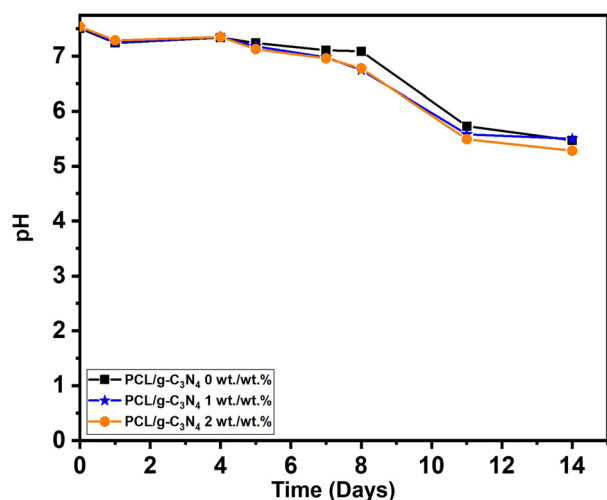
to pH values within the range of 5.2–5.5, while a higher g-C$_3$N$_4$ content gives rise to slightly lower final pH values. The observed pH variations have significant consequences concerning biomedical applications, such as in neural tissue engineering. While the initial pH values fall within the physiological range, the gradual acidification may affect cell viability and tissue response.[93,94] On the other hand, the relatively low rate at which pH changes take place could provide sufficient time for cellular adaptation mechanisms to balance changes in the environmental conditions.

3.4. Anti-biofouling activity against bacteria

Fig. 9 presents the microscopic investigation of pristine, PCL, and PCL/g-C$_3$N$_4$ coated ALNPMs before and after exposure to the suspensions of microbial species *S. aureus*, *E. coli* and *C. albicans*. The anti-biofouling properties of the membranes were investigated by static contact experiments using the live viability assay. Results demonstrated that the pristine ALNPM showed significant microbial adhesion, which is visible through many dark spots distributed across the surface, as indicated by the dense growth of microbes on this membrane.

In contrast, PCL coated membranes grafted with different NHS/EDC ratios showed various levels of antimicrobial activity. The grafted PCL membranes with NHS : EDC ratios of 1 : 1.5 and 2 : 3 showed only moderate inhibition of *E. coli* and *S. aureus* and less effective inhibition against the growth of *C. albicans*. Among them, the addition of 1 wt% g-C$_3$N$_4$ to the PCL coating matrix with different NHS/EDC ratios (*i.e.* 1 : 1.5 and 2 : 3) resulted in higher antimicrobial activity against all three microbes, especially against *E. coli* and *S. aureus*, showing that the g-C$_3$N$_4$ incorporation in the PCL coating further enhanced its antifouling properties.

Finally, among these coatings, the PCL/2 wt% g-C$_3$N$_4$ coated membrane grafted with an NHS : EDC ratio of 2 : 3 was the most effective against all three microbial isolates, which implied that PCL/2 wt% g-C$_3$N$_4$ grafting onto the membrane significantly inhibited microbial growth, as shown in Fig. 9. Based on the obtained results, theoretically g-C$_3$N$_4$ enhances PCL membrane coatings through the dual modes of antimicrobial and antifouling mechanisms. Photocatalytically, it generates reactive oxygen species such as superoxide and hydroxyl radicals that destroy bacterial cell membranes and induce oxidative stress.[89–92] Simultaneously, modification of the surface hydrophilicity reduces protein adsorption and bacterial adhesion due to the creation of an unfavorable environment for microbial colonization. The special electronic structure of this material can generate electron–hole pairs under light irradiation, converting oxygen into radicals and efficiently inhibiting biofilm formation while keeping the membranes in a sterile state.[93,94]

3.5. Adsorption of bovine serum albumin

The adsorption of BSA protein onto the surface of ALNPMs coated with PCL and a PCL/g-C$_3$N$_4$ composite changes from 2 hours to 14 days, indicating potential antifouling performance issues that are common in many applications, as shown in Fig. 10. The pristine ALNPM (black bars) shows strong positive

Fig. 8 pH profiles *versus* time over 14 days for ALNPMs coated with three different compositions of PCL composites.

BSA binding during the test period. At 0.083 days (approximately 2 hours), the adsorption rate is approximately 85%, indicating strong protein adhesion to the bare aluminum surface.
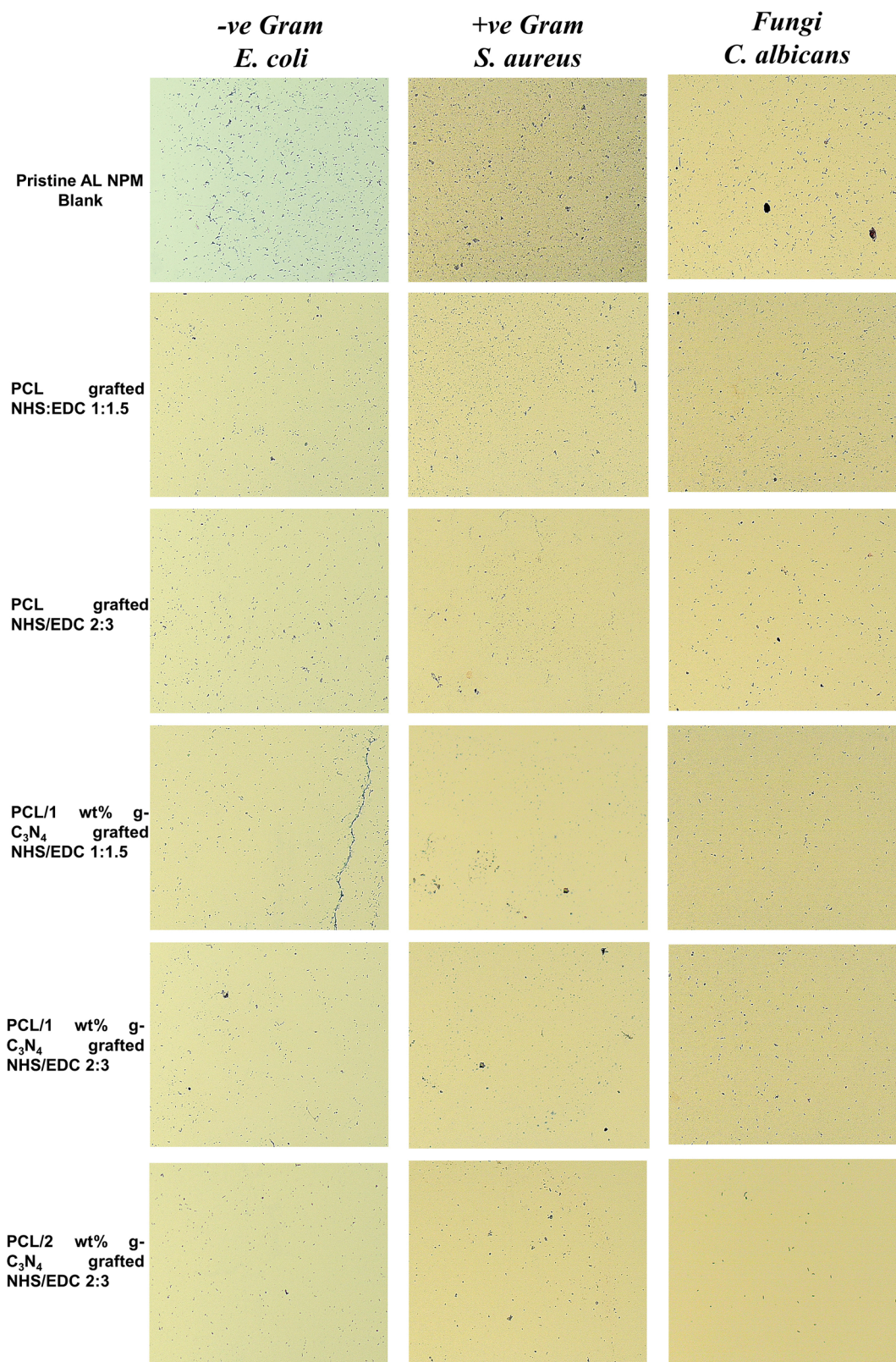
Fig. 9 The alumina nanoporous membrane (ALNPMs) before and after different treatments of the coatings exposed to *S. aureus*, *E. coli* and *C. albicans*.

This high protein adsorption is expected on untreated metal surfaces since such surfaces possess high surface energy and protein-favorable character.[2,95] The adsorption on ALNPMs decreases gradually over time to approximately 55% on day 1, falling to values around 70% on days 4 and 7, dropping further to approximately 67% on day 11, and subsequently to around 30% by day 14. This trend may be attributed to protein saturation effects, where proteins that are adsorbed early are subjected to conformational changes or degradation, resulting in decreased measured adsorption with longer exposure times.[96,97]

The PCL coating (red bars) exhibits more consistent performance over time. Initial adsorption is around 77% at 2 hours, lower than that of uncoated ALNPMs, which indicates some direct antifouling benefits. Adsorption decreases gradually over the 14 days, reaching around 50% on day 14. While PCL typically outperforms uncoated ALNPMs in long-term antifouling performance, the composite coatings dominate during the short-term exposure period. The time-dependent enhancement of the antifouling character suggests that the PCL coating undergoes favorable structural arrangements with longer exposure to the aqueous environment, perhaps transforming into an improved protein-repellent surface over time.[98,99] Previous research has demonstrated that PCL can exhibit moderate antifouling properties due to its semicrystalline nature and hydrophobicity.[100]

The antifouling performance of the PCL/1 wt% g-C$_3$N$_4$ composite coating (blue bars) is superior to that of the uncoated ALNPMs and PCL coating. The protein adsorption rate of ~80% at 2 hours is comparable to that of the other coatings, but with greater stability for the test duration. Notably, this coating performs better than uncoated PCL at each time point between day 1 and day 11, with protein adsorption values remaining consistent in the range of 60–75%. On day 14, adsorption falls to approximately 48%, similar to the PCL coating. This sustained performance indicates that the addition of 1 wt% g-C$_3$N$_4$ enhances the protein fouling resistance of the coating, which may be due to the hydrophilic nature and unique electronic properties of g-C$_3$N$_4$ hindering protein–surface interactions.[101–103]

The most captivating behavior was observed for the PCL/2 wt% g-C$_3$N$_4$ composite coating (purple bars). It exhibits the highest initial adsorption of BSA at around 92% within 2 hours, which suggests strong protein binding to the surface initially. The coating also exhibits the greatest decline in adsorption over time to merely around 28% on day 14, the lowest among all tested coatings. This dramatic enhancement in antifouling capabilities over time suggests that this coating may undergo favorable surface restructuring or conditioning upon exposure to the protein solution. The higher concentration of g-C$_3$N$_4$ may create a more hydrophilic surface upon initial exposure, subsequently being able to decrease protein adhesion more effectively than the other coatings.

This outstanding performance indicates that increasing the g-C$_3$N$_4$ content to 2 wt% significantly enhances the antifouling performance of the composite coating, showing the strongest
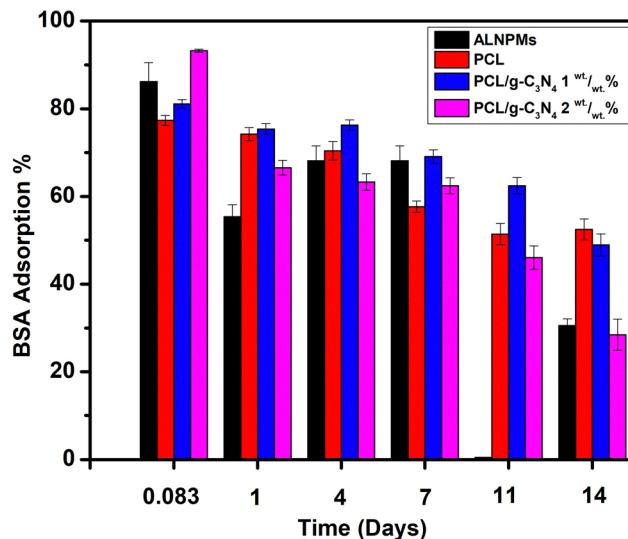

Fig. 10 Antifouling activity based on BSA adsorption on pristine ALNPMs and ALNPMs coated with PCL, PCL/1 wt% g-C$_3$N$_4$ and PCL/2 wt% g-C$_3$N$_4$.

protein repulsion among the tested materials.[104] The concentration-dependent improvement agrees with observations from several studies that have investigated the optimal loading of nanomaterials in polymer composites for enhanced functionality.[15,16]

The antifouling activity of PCL and PCL/g-C$_3$N$_4$ composite coatings is attributed to a combination of synergistic mechanisms: the optimal hydrophilicity/hydrophobicity ratio provided by PCL and further enhanced by g-C$_3$N$_4$ results in a surface energy state that reduces protein interactions;[30,105] the nitrogen-rich skeleton of g-C$_3$N$_4$ forms a protective hydration layer through hydrogen bonding with water, forming an impenetrable physical barrier for protein adsorption;[37,39,106] the inclusion of g-C$_3$N$_4$ nanoparticles brings surface charges that electrostatically repel negatively charged BSA proteins;[107,108] the composite coatings form an unusual topography unfavorable for protein attachment, with the 2 wt% loading providing optimal surface morphology;[109] and all coatings exhibit a time-dependent enhancement of antifouling performance due to beneficial structural arrangement upon prolonged aqueous exposure, with g-C$_3$N$_4$-containing composites exhibiting greatest improvements.[110,111]

3.6. Antibacterial efficacy

The antibacterial activity of ALNPMs coated with either PCL or the PCL/g-C$_3$N$_4$ composite has been investigated as shown in Table 1. The inhibition zone is one of the most important factors determining the antibacterial efficacy of materials; a larger inhibition zone indicates stronger antibacterial activity. The table shows that PCL membranes without g-C$_3$N$_4$ (*i.e.* PCL grafted with NHS : EDC ratios of 1 : 1.5 and 2 : 3) displayed moderate antibacterial activity, whose inhibition zones were 16 and 14 mm for *S. aureus* and 20 and 16 mm for *E. coli*, respectively. The addition of g-C$_3$N$_4$ in PCL enhanced the antibacterial efficacy, as observed for samples PCL/1 wt% g-C$_3$N$_4$ grafted with NHS : EDC ratios of 1 : 1.5 and 2 : 3 and

PCL/2% C_3N_4 grafted with an NHS : EDC ratio of 2 : 3. For example, PCL with 1 wt% g-C_3N_4 showed inhibition zones of 25 mm for *S. aureus* and 30 mm for *E. coli*, reflecting a highly enhanced antimicrobial performance of the samples compared to PCL only. Among these, PCL/2 wt% g-C_3N_4 exhibited the highest antibacterial activity, and its inhibition zones for *S. aureus* and *E. coli* were 30 and 36 mm, respectively (see Table 1).

These improved antibacterial properties of PCL/g-C_3N_4 membranes could be attributed to several mechanisms: (i) the incorporation of g-C_3N_4 increases the surface roughness and might cause physical disruption of bacterial membranes upon contact, leading to cell lysis. In addition, the photocatalytic properties of g-C_3N_4 initiate ROS generation under visible light irradiation. The produced ROS can cause oxidative stress in bacteria by damaging bacterial DNA, proteins, and lipid membranes, leading to eventual cell death.[89–92] Another mechanism is based on the synergistic effect of NHS : EDC grafting, which enhances the structural stability of PCL membranes themselves and potentially further enhances interactions with bacterial cells, contributing more to the antimicrobial activity.[112,113]

These results show that Gram-negative *E. coli* bacteria are slightly more vulnerable to PCL/g-C_3N_4 coatings than Gram-positive *S. aureus*. Probably, this difference may be linked with the cell wall structure. In fact, Gram-negative bacteria have an outer membrane made up of lipopolysaccharides that may be more vulnerable to oxidative damage caused by ROS. On the other hand, Gram-positive bacteria have a thick peptidoglycan layer that can help protect them in some ways.[114]

The enhanced antibacterial activity observed for the PCL/g-C_3N_4 coatings can be attributed to the synergistic mechanism of physical membrane disruption and photocatalytic ROS generation.[115,116] The surface morphology characterized by SEM revealed nano-roughened textures arising from the incorporation of g-C_3N_4 nanosheets, which are known to facilitate bacterial cell wall damage upon contact. Similar contact-induced physical disruption has been previously documented for g-C_3N_4-based nanostructures with analogous morphologies.[117]

The pronounced antibacterial inhibition zones ($\sim$30–36 mm) obtained under ambient illumination confirm the contribution of photocatalytic ROS generation, as widely reported for g-C_3N_4 systems. Ding *et al.* demonstrated that graphitic carbon nitride effectively inactivates both *E. coli* and

S. aureus through light-induced superoxide ($^\bullet O_2^-$) and hydroxyl radical ($^\bullet OH$) generation without the need for additional fluorescent-probe confirmation.[118]

Leng *et al.* further confirmed that chemically modified g-C_3N_4 exhibits enhanced bacterial interactions and ROS formation under visible light, leading to near-complete cell collapse visible through SEM.[117]

Yang *et al.* also verified the same mechanism through fluorescence live/dead imaging, showing that g-C_3N_4 photocatalysts cause rapid conversion of live (SYTO9-positive) to dead (PI-positive) cells upon light exposure.[119]

In line with these findings, the markedly increased antibacterial efficacy of the 2 wt% g-C_3N_4–PCL coating, relative to the control PCL, provides indirect but well-established evidence of the involvement of photocatalytic ROS.[120] Therefore, while techniques such as DCFH-DA fluorescence or PI staining are valuable, the current morphological, antibacterial, and comparative results—together with extensive corroborating literature—are sufficient to substantiate the proposed dual mechanism of physical destruction and photocatalysis without additional confirmatory experiments.

3.7. Biomedical relevance and comparative assessment

The biomedical use of the synthesized PCL/g-C_3N_4-coated alumina nanoporous membranes (ALNPMs) is attributed to their combined antifouling, antibacterial, and pH-stable characteristics under physiological conditions, which make them potential candidates for applications in implantable devices, neural interfaces, wound dressings, and extracorporeal filtration systems. Their enhanced hydrophilicity and considerably reduced protein adsorption ($\sim$28% within 14 days) minimize nonspecific bio-adhesion, thereby inhibiting biofilm formation and immune rejection upon exposure to biological fluids. The coatings were also stable at the pH of artificial cerebrospinal fluid (A-CSF, $\sim$7.2–7.4), reiterating their effectiveness for the sensitive neural and intracorporeal settings.

Compared to conventional PEGylated or zwitterionic polymer coatings that passively inhibit protein adsorption *via* the formation of hydration layers,[105,121,122] the PCL/g-C_3N_4 system introduces an active, visible light-induced antibacterial mechanism. The photocatalytic g-C_3N_4 domain generates reactive oxygen species (ROS) upon visible light irradiation, facilitating self-sterilisation without metal leakage.[90,91] This aspect distinguishes the present coating from Ag- and TiO_2-based systems,

---

Table 1 Antibacterial activity of PCL and PCL/g-C_3N_4 coated ALNPMs against Gram-positive and Gram-negative bacterial isolates in terms of the inhibition zone

Sample	Pathogens	
	Gram-positive	Gram-negative
	Staphylococcus aureus (ATCC-29213)	*Escherichia coli* (ATCC-25922)
PCL grafted with an NHS : EDC ratio of 1 : 1.5	16 ± 0.8 mm	20 ± 1.0 mm
PCL grafted with an NHS : EDC ratio of 2 : 3	14 ± 0.7 mm	16 ± 0.8 mm
PCL/1% C_3N_4 grafted with an NHS : EDC ratio of 1 : 1.5	25 ± 1.25 mm	30 ± 1.5 mm
PCL/1% C_3N_4 grafted with an NHS : EDC ratio of 2 : 3	28 ± 1.4 mm	34 ± 0.7 mm
PCL/2% C_3N_4 grafted with an NHS : EDC ratio of 2 : 3	30 ± 1.5 mm	36 ± 1.8 mm

respectively, based on ion release or UV activation—both cytotoxicity- and/or practicability-limited. The visible light activation of g-C$_3$N$_4$ (band-gap $\approx$ 2.7 eV) provides biocompatibility for biomedical applications and enables sustainable, on-demand surface sanitation.[101]

Notably, the composite coatings showed inhibition zones of 30–36 mm against *S. aureus* and *E. coli*, which is superior to pure PCL and comparable to or better than Ag-based analogues, without ion-leaching toxicity. Because PCL is biocompatible and biodegradable, the matrix gradually integrates or can resorb *in vivo*, whereas g-C$_3$N$_4$ maintains structural and antimicrobial activity. Consequently, the PCL/g-C$_3$N$_4$ hybrid presents a metal-free, self-sterilising, two-way surface that involves long-term antifouling and photocatalytic antibacterial functions and is a prime contender for future implantable coatings and biomedical membranes.

4. Conclusions

The current study demonstrates the enhanced antifouling and antibacterial properties of ALNPMs after coating with PCL/g-C$_3$N$_4$ coatings. Loading of g-C$_3$N$_4$ increases the hydrophilicity of the coating, reduces protein adsorption, and enhances bacterial inhibition. The 2 wt% g-C$_3$N$_4$ coated ALNPMs exhibited the best performance, with the greatest reduction in fouling and strong antibacterial activity against *E. coli* and *S. aureus*. Some of the improvements providing for the reduction of microbial adhesion are increased surface roughness, the generation of reactive oxygen species, and hydrophilic interactions. The present work describes the possibility of using PCL/g-C$_3$N$_4$ coatings for advanced membrane applications as a sustainable solution for biomedical applications.

Author contributions

ANE (Ahmed Nabile Emam): conceptualization, methodology, characterization, validation, formal data analysis, investigation, and writing of the original draft and editing of the final version of the manuscript till submission and acceptance for publication; LO (Lamyaa Osama): methodology, characterization, formal data analysis, and investigation; HHB (Hanan Hassan Beherei): resources, project administration and funding acquisition; MM (Mostafa Mabrouk): resources, data curation, writing – review and editing of the final version of the manuscript, supervision, project administration and funding acquisition. All authors have read and agreed to the published version of the manuscript.

Conflicts of interest

There are no conflicts to declare.

Data availability

The authors confirm that the data supporting the findings of this study are available within the article.

Acknowledgements

Notes and references

1 H. Zhang and M. Chiao, *J. Med. Biol. Eng.*, 2015, **35**, 143–155.
2 A. Abdelrasoul, H. Doan, A. Lohi and C.-H. Cheng, *Osmotically Driven Membrane Processes: Approach, Development and Current Status*, 2018, pp. 151–177.
3 S. Liu and W. Guo, *Adv. Funct. Mater.*, 2018, **28**, 1800596.
4 J. L. Harding and M. M. Reynolds, *Trends Biotechnol.*, 2014, **32**, 140–146.
5 A. Asad, D. Sameoto and M. Sadrzadeh, *Nanocomposite membranes for water and gas separation*, Elsevier, 2020, pp. 1–28.
6 R. W. Baker, *Membrane technology and applications*, John Wiley & Sons, 2023.
7 Y.-R. Chang, Y.-J. Lee and D.-J. Lee, *J. Taiwan Inst. Chem. Eng.*, 2019, **94**, 88–96.
8 K. Khoiruddin, R. Boopathy, S. Kawi and I. Wenten, *Curr. Pollut. Rep.*, 2025, **11**, 15.
9 Z. Wang, A. Knebel, S. Grosjean, D. Wagner, S. Bräse, C. Wöll, J. Caro and L. Heinke, *Nat. Commun.*, 2016, **7**, 13872.
10 P. Stroeve and N. Ileri, *Trends Biotechnol.*, 2011, **29**, 259–266.
11 M. Sun, K. Han, R. Hu, D. Liu, W. Fu and W. Liu, *Adv. Healthcare Mater.*, 2021, **10**, 2001545.
12 A. Priya, L. Gnanasekaran, P. S. Kumar, A. Jalil, T. K. Hoang, S. Rajendran, M. Soto-Moscoso and D. Balakrishnan, *Chemosphere*, 2022, **303**, 135205.
13 Y. Wang, B. Ma, M. Ulbricht, Y. Dong and X. Zhao, *Water Res.*, 2022, **226**, 119173.
14 K. P. Lee, University of Bath, 2013.
15 H. Singh, P. Saxena and Y. Puri, *CIRP J. Manuf. Sci. Technol.*, 2021, **33**, 339–368.
16 M. Moaness, S. A. M. El-Sayed, H. H. Beherei and M. Mabrouk, *J. Funct. Biomater.*, 2024, **15**, 50.
17 K. Peng Lee and D. Mattia, *J. Membr. Sci.*, 2013, **435**, 52–61.
18 M. Aramesh and J. Cervenka, *Nanomedicine*, 2014, **438**, 438.
19 C.-W. Chu and C.-H. Tsai, *Langmuir*, 2024, **40**, 5245–5254.
20 S. W. Lee, H. Shang, R. T. Haasch, V. Petrova and G. U. Lee, *Nanotechnology*, 2005, **16**, 1335.
21 A. S. González, V. Vega, A. L. Cuevas, M. D. V. M. D. Yuso, V. M. Prida and J. Benavente, *Materials*, 2021, **14**, 5052.
22 N. L. Bragazzi, R. Gasparini, D. Amicizia, D. Panatto and C. Larosa, *Adv. Protein Chem. Struct. Biol.*, 2015, **101**, 213–229.
23 M. Singh and G. Das, *IOSR J. Appl. Chem.*, 2014, **7**, 17–34.

24 T. G. Schreiner, B. I. Tamba, C. T. Mihai, A. Lőrinczi, M. Baibarac, R. C. Ciobanu and B. O. Popescu, *J. Clin. Med.*, 2022, **11**, 5846.

25 L. Osama, H. T. Handal, S. A. El-Sayed, E. M. Elzayat and M. Mabrouk, *Nanomaterials*, 2024, **14**, 1078.

26 M. M. Pendergast and E. M. Hoek, *Energy Environ. Sci.*, 2011, **4**, 1946–1971.

27 X. Zhao, H. Xuan, Y. Chen and C. He, *J. Membr. Sci.*, 2015, **494**, 48–56.

28 J. Xu, Z. Wang, J. Wang and S. Wang, *Desalination*, 2015, **365**, 398–406.

29 A. M. C. Maan, A. H. Hofman, W. M. de Vos and M. Kamperman, *Adv. Funct. Mater.*, 2020, **30**, 2000936.

30 I. Banerjee, R. C. Pangule and R. S. Kane, *Adv. Mater.*, 2011, **23**, 690–718.

31 Y. Gu, L. Yu, J. Mou, D. Wu, M. Xu, P. Zhou and Y. Ren, *Mar. Drugs*, 2020, **18**, 371.

32 Y. Wang, D. Hao, M. Yang, X. Su, P. Li, Q. Liu and X. Guo, *Prog. Org. Coat.*, 2022, **173**, 107225.

33 M. Darya, M. H. Abdolrasouli, M. Yousefzadi, M. M. Sajjadi, I. Sourinejad and M. Zarei, *AMB Express*, 2022, **12**, 24.

34 C. Ma, W. Zhang, G. Zhang and P.-Y. Qian, *ACS Sustainable Chem. Eng.*, 2017, **5**, 6304–6309.

35 W. Li, Y. Zong, Q. Liu, Y. Sun, Z. Li, H. Wang and Z. Li, *Prog. Org. Coat.*, 2020, **147**, 105776.

36 J. Yao, S. Chen, C. Ma and G. Zhang, *J. Mater. Chem. B*, 2014, **2**, 5100–5106.

37 J. Hou, S. Liu, X. Jiang, G. I. Waterhouse, Z.-M. Zhang and L.-M. Yu, *Prog. Org. Coat.*, 2021, **154**, 106203.

38 F. Guo, L. Li, Y. Shi, W. Shi, X. Yang and H. Li, *Prog. Org. Coat.*, 2023, **179**, 107512.

39 F. Yang, G. Ding, J. Wang, Z. Liang, B. Gao, M. Dou, C. Xu and S. Li, *J. Membr. Sci.*, 2020, **606**, 118146.

40 Z. Zhang, Y. Li, R. Chen, Q. Liu, J. Liu, J. Yu, H. Zhang, D. Song and J. Wang, *New J. Chem.*, 2021, **45**, 780–787.

41 S. Remanan, M. Sharma, S. Bose and N. C. Das, *ChemistrySelect*, 2018, **3**, 609–633.

42 R. Sachan, S. G. Warkar and R. Purwar, *Polym.-Plast. Technol. Mater.*, 2023, **62**, 327–358.

43 J. U. Pothupitiya, C. Zheng and W. M. Saltzman, *Expert Opin. Drug Delivery*, 2022, **19**, 1351–1364.

44 D. Valerini, L. Tammaro, R. Vitali, G. Guillot and A. Rinaldi, *Coatings*, 2021, **11**, 345.

45 G. Ö. Kayan and A. Kayan, *Chem. Eng.*, 2023, **7**, 104.

46 B. Li, B. Qi, J. Han, C. Yang, X. Qian and T. Jiao, *Colloids Surf., A*, 2024, **693**, 134088.

47 A. Joy, G. Unnikrishnan, M. Megha, M. Haris, J. Thomas, E. Kolanthai and S. Muthuswamy, *J. Inorg. Organomet. Polym. Mater.*, 2022, **32**, 912–930.

48 S. Awasthi and S. K. Pandey, *Appl. Mater. Today*, 2024, **36**, 102058.

49 J. A. S. Syed, X.-Y. Zhang, W.-J. Ding and A.-D. Li, *J. Environ. Chem. Eng.*, 2022, **10**, 108745.

50 N. S. Prasanna, N. Choudhary, N. Singh and K. Raghavarao, *Chem. Eng. J. Adv.*, 2023, **14**, 100486.

51 W. Zhang, S. Zhang, C. Meng and Z. Zhang, *Appl. Catal., B*, 2023, **322**, 122098.

52 S. M. Hosseini and V. Safarifard, *Surf. Interfaces*, 2024, **55**, 105399.

53 S. Davies, M. Baumann, S. Byun, L. Corneal, V. Tarabara and S. Masten, *Water Sci. Technol.: Water Supply*, 2010, **10**(1), 81–86.

54 H. Saleem, S. J. Zaidi, A. F. Ismail, P. S. Goh and A. Vinu, *Desalination*, 2022, **542**, 116061.

55 T. Wang, B. Song and L. Wang, *Polymers*, 2020, **12**(1), 76.

56 M. Taha, A. Khalid, M. G. Elmahgary, S. S. Medany and Y. A. Attia, *Sci. Rep.*, 2024, **14**, 4184.

57 M. Waheed, A. N. Emam and G. G. Mohamed, *Egypt. J. Chem.*, 2024, **68**(6), 431–450.

58 J. Huang, M. Klahn, X. Tian, X. Dai, J. Rabeah, V. Aladin, B. Corzilius, S. Bartling, H. Lund, N. Steinfeldt, T. Peppel, A. J. Logsdail, H. Jiao and J. Strunk, *ACS Appl. Nano Mater.*, 2024, **7**, 7442–7452.

59 M. Moaness, S. A. El-Sayed, H. H. Beherei and M. Mabrouk, *J. Funct. Biomater.*, 2024, **15**, 50.

60 X.-X. Ni, J.-H. Li and L.-P. Yu, *Mater. Adv.*, 2021, **2**, 3300–3314.

61 W. Xu, H. Zhuang, Z. Xu, M. Huang, S. Gao, Q. Li and G. Zhang, *Adv. Polym. Technol.*, 2020, **2020**, 5456707.

62 S. Akhshabi, E. Biazar, V. Singh, S. H. Keshel and N. Geetha, *Int. J. Nanomed.*, 2018, 4405–4416.

63 J. McFARLAND, *JAMA, J. Am. Med. Assoc.*, 1907, **XLIX**, 1176–1178.

64 L. Lahuerta Zamora and M. T. Pérez-Gracia, *J. R.Soc., Interface*, 2012, **9**, 1892–1897.

65 M. Elgayyar, F. A. Draughon, D. A. Golden and J. R. Mount, *J. Food Prot.*, 2001, **64**, 1019–1024.

66 C. Perez, *Acta Biol. Med. Exp.*, 1990, **15**, 113–115.

67 S. P. Pattnaik, A. Behera, S. Martha, R. Acharya and K. Parida, *J. Mater. Sci.*, 2019, **54**, 5726–5742.

68 F. Fina, S. K. Callear, G. M. Carins and J. T. S. Irvine, *Chem. Mater.*, 2015, **27**, 2612–2618.

69 Y. Boushi and T. Yanagishita, *Langmuir*, 2024, **40**, 5278–5287.

70 S. Manzoor, M. W. Ashraf, S. Tayyaba and M. K. Hossain, *arXiv, preprint*, arXiv:2112.08450, 2021.

71 W. Lee and S.-J. Park, *Chem. Rev.*, 2014, **114**, 7487–7556.

72 D. L. Schmidt, R. F. Brady, K. Lam, D. C. Schmidt and M. K. Chaudhury, *Langmuir*, 2004, **20**, 2830–2836.

73 X. Lu, Y. Peng, H. Qiu, X. Liu and L. Ge, *Desalination*, 2017, **413**, 127–135.

74 L. Fan, Q. Zhang, Z. Yang, R. Zhang, Y.-N. Liu, M. He, Z. Jiang and Y. Su, *ACS Appl. Mater. Interfaces*, 2017, **9**, 13577–13586.

75 D. Ahmad, V. D. B. Inge, M. Jeremey, P. Roy and H. Jouhara, *Energy Sources, Part A*, 2018, **40**, 2686–2725.

76 D. Rana and T. Matsuura, *Chem. Rev.*, 2010, **110**, 2448–2471.

77 M. Koenig and S. Huang, *Polym. Degrad. Stab.*, 1994, **45**, 139–144.

78 J. Ayyavoo, T. P. N. Nguyen, B.-M. Jun, I.-C. Kim and Y.-N. Kwon, *Colloids Surf., A*, 2016, **506**, 190–201.

79 V. Vatanpour, S. Paziresh, A. Dehqan, S. Asadzadeh-Khaneghah and A. Habibi-Yangjeh, *Chemosphere*, 2021, **279**, 130616.

80 A. Ostovar, M. Tarkhani, S. A. Mousavi and M. Asadollahi, *Polym. Eng. Sci.*, 2024, **64**, 565–576.

81 H. S. Sundaram, X. Han, A. K. Nowinski, N. D. Brault, Y. Li, J. R. Ella-Menye, K. A. Amoaka, K. E. Cook, P. Marek and K. Senecal, *Adv. Mater. Interfaces*, 2014, **1**, 1400071.

82 Y. Wang, D. E. Betts, J. A. Finlay, L. Brewer, M. E. Callow, J. A. Callow, D. E. Wendt and J. M. DeSimone, *Macromolecules*, 2011, **44**, 878–885.

83 M. Al-Shaeli, S. J. Smith, E. Shamsaei, H. Wang, K. Zhang and B. P. Ladewig, *RSC Adv.*, 2017, **7**, 37324–37330.

84 W. Liu, C. Su, P. Su, H. Yang, P. Lu, Z. Du and Y. Ye, *Macromol. Mater. Eng.*, 2021, **306**, 2100026.

85 C. Chen, Y. He, G. Xiao, F. Zhong, Y. Xia and Y. Wu, *Prog. Org. Coat.*, 2020, **139**, 105448.

86 D. Al Mais, S. Mustapha, Y. N. Baghdadi, K. Bouhadir and A. R. Tehrani-Bagha, *Polymers*, 2024, **16**(13), 1935.

87 N. E. Zikalala, S. A. Zikalala, S. Azizi, I. A. Kamika, E. N. Nxumalo, A. A. Zinatizadeh, E. M. N. Chirwa and M. Maaza, *Ind. Eng. Chem. Res.*, 2023, **62**, 9354–9380.

88 M. A. Ahmed, S. A. Mahmoud and A. A. Mohamed, *RSC Adv.*, 2024, **14**, 18879–18906.

89 J. Guo, J. Zhou, Z. Sun, M. Wang, X. Zou, H. Mao and F. Yan, *Acta Biomater.*, 2022, **146**, 370–384.

90 R. Li, Y. Ren, P. Zhao, J. Wang, J. Liu and Y. Zhang, *J. Hazard. Mater.*, 2019, **365**, 606–614.

91 C. Zhang, Y. Li, D. Shuai, Y. Shen, W. Xiong and L. Wang, *Chemosphere*, 2019, **214**, 462–479.

92 L. Qi, Y. Yang, Z. Yang, J. Qi, Y. Zhou, Z. Zhu and J. Li, *Water Res.*, 2025, **268**, 122581.

93 W. Ma, J. Pan, W. Ren, L. Chen, L. Huang, S. Xu and Z. Jiang, *J. Membr. Sci.*, 2022, **659**, 120792.

94 X. Li, G. Huang, X. Chen, J. Huang, M. Li, J. Yin, Y. Liang, Y. Yao and Y. Li, *Sci. Total Environ.*, 2021, **792**, 148462.

95 J. Andrade and V. Hlady, *Biopolymers/Non-Exclusion HPLC*, 2005, pp. 1–63.

96 W. Norde, *Colloids Surf., B*, 2007, **61**, 1–9.

97 M. Rabe, D. Verdes and S. Seeger, *Adv. Colloid Interface Sci.*, 2011, **162**, 87–106.

98 J. Wen, S. Huang, Q. Hu, W. He, Z. Wei, L. Wang, J. Lu, X. Yue, S. Men and C. Miao, *Mater. Today Chem.*, 2024, **40**, 102232.

99 Y.-Q. Zhao, J.-H. Yang, X. Ding, X. Ding, S. Duan and F.-J. Xu, *Bioact. Mater.*, 2020, **5**, 185–191.

100 J. M. Goddard and J. Hotchkiss, *Prog. Polym. Sci.*, 2007, **32**, 698–725.

101 W.-J. Ong, L.-L. Tan, Y. H. Ng, S.-T. Yong and S.-P. Chai, *Chem. Rev.*, 2016, **116**, 7159–7329.

102 Y. Wen, J. Yuan, X. Ma, S. Wang and Y. Liu, *Environ. Chem. Lett.*, 2019, **17**, 1539–1551.

103 S. Pourhashem, A. Seif, F. Saba, E. G. Nezhad, X. Ji, Z. Zhou, X. Zhai, M. Mirzaee, J. Duan and A. Rashidi, *J. Mater. Sci. Technol.*, 2022, **118**, 73–113.

104 V. Kochkodan and N. Hilal, *Desalination*, 2015, **356**, 187–207.

105 S. Chen, L. Li, C. Zhao and J. Zheng, *Polymer*, 2010, **51**, 5283–5293.

106 S. Chen, J. Zheng, L. Li and S. Jiang, *J. Am. Chem. Soc.*, 2005, **127**, 14473–14478.

107 E. Ostuni, R. G. Chapman, R. E. Holmlin, S. Takayama and G. M. Whitesides, *Langmuir*, 2001, **17**, 5605–5620.

108 J. C. Hower, Y. He, M. T. Bernards and S. Jiang, *J. Chem. Phys.*, 2006, **125**(21), 214704.

109 A. T. Nguyen, S. R. Sathe and E. K. Yim, *J. Phys.: Condens. Matter*, 2016, **28**, 183001.

110 C. Leng, H. G. Buss, R. A. Segalman and Z. Chen, *Langmuir*, 2015, **31**, 9306–9311.

111 J. B. Schlenoff, *Langmuir*, 2014, **30**, 9625–9636.

112 P. M. Costa, D. A. Learmonth, D. B. Gomes, M. P. Cautela, A. C. Oliveira, R. Andrade, J. Espregueira-Mendes, T. R. Veloso, C. B. Cunha and R. A. Sousa, *Polymers*, 2021, **13**, 3317.

113 Y. Campos, F. J. Sola, G. Fuentes, L. Quintanilla, A. Almirall, L. J. Cruz, J. C. Rodríguez-Cabello and Y. Tabata, *Polymers*, 2021, **13**, 907.

114 N. El-Kattan, A. N. Emam, A. S. Mansour, M. A. Ibrahim, A. B. Abd El-Razik, K. A. Allam, N. Y. Riad and S. A. Ibrahim, *RSC Adv.*, 2022, **12**, 18022–18038.

115 C. Zhang, Y. Li, C. Wang and X. Zheng, *Sci. Total Environ.*, 2021, **755**, 142588.

116 L. Lin, Z. Su, Y. Li and C. Zhang, *Chemosphere*, 2021, **265**, 129060.

117 J. Leng, X. Liu, Y. Xu, S.-E. Zhu, Y. Zhang, Z. Tan, X. Yang, J.-E. Jin, Y. Shi and H. Fan, *J. Mater. Chem. B*, 2025, **13**, 264–273.

118 N. Ding, X. Chang, N. Shi, X. Yin, F. Qi and Y. Sun, *Environ. Sci. Pollut. Res.*, 2019, **26**, 18730–18738.

119 X. Yang, L. Sheng, Y. Ye, J. Sun, S. Geng, D. Ning, Y. Zhang and X. Sun, *Chem. Eng. J.*, 2023, **474**, 145771.

120 N. Shen, X. Wu, D. Li, H. Lin, D. Xu and M. Chen, *J. Photochem. Photobiol., A*, 2024, **455**, 115784.

121 H. Yang, Y. Wang, L. Yao, J. Wang and H. Chen, *Langmuir*, 2025, **41**, 6471–6496.

122 Q. Li, C. Wen, J. Yang, X. Zhou, Y. Zhu, J. Zheng, G. Cheng, J. Bai, T. Xu and J. Ji, *Chem. Rev.*, 2022, **122**, 17073–17154.